Check for updates

Advanced Functional Materials

ADVANCED FUNCTIONAL MATERIALS
www.afm-journal.de

RESEARCH ARTICLE

Dual-Mode Photoresponse via Photoconductive and Thermally Induced Interfacial Modulation in MoS_2/Perovskite Heterostructures

Jiaqi Tang[1,2,3] | Dongdong Zhao[2] | Kaiyu Hu[2] | Yepei Mo[1,2,3] | Qijian Wang[2] | Xiaojun Pan[1,2] | Jiaqi He[1,3] | Zeping He[1,3] | Jia Long[2] | Yu Zhang[2] | Jiarun Ding[1,2,3] | Wenchao Gao[1] | Zhifang Liu[2] | Muhong Wu[2] | Caofeng Pan[2,3]

[1]Beijing Institute of Nanoenergy and Nanosystems, Chinese Academy of Sciences, Beijing, P. R. China | [2]Beijing Key Laboratory for Atomic Manufacturing Equipment and Intelligent Sensing, Institute of Atomic Manufacturing, Beihang University, Beijing, P. R. China | [3]School of Nanoscience and Engineering, University of Chinese Academy of Sciences, Beijing, P. R. China

Correspondence: Wenchao Gao (gaowenchao@binn.cas.cn) | Zhifang Liu (liuzhifang@buaa.edu.cn) | Muhong Wu (muhongwu@buaa.edu.cn) | Caofeng Pan (pancaofeng@buaa.edu.cn)

Received: 7 February 2026 | **Revised:** 22 May 2026 | **Accepted:** 3 June 2026

Keywords: dual-mode photodetector | heterojunction | MoS_2/$MAPbBr_3$ | photoconductive effect | thermally induced response

ABSTRACT

Next-generation optoelectronic systems demand photodetectors capable of both wavelength-dependent and spectrally selective response, particularly under low-light or long-wavelength conditions. Conventional photodetectors based on a single photoresponse mechanism face inherent limitations in dual-mode photoresponse and wavelength discrimination capability. Herein, we report a dual-mode photodetector that integrates photoconductive and thermally induced transient responses within a monolayer MoS_2/$MAPbBr_3$ perovskite heterostructure. Under a low external bias, green light induces a steady-state photoconductive current in the MoS_2 channel, while red light triggers a transient current induced by thermally driven interfacial modulation at the MoS_2/$MAPbBr_3$ interface. This wavelength-dependent dual-response enables intrinsic spectral selectivity and signal discrimination. Leveraging these coupled dynamics, the device demonstrates real-time recognition of red-green optical numeric patterns via a simple signal classification protocol. Our findings unveil the synergistic interplay between photoconductive and thermally induced mechanisms in TMD-perovskite hybrids, offering a promising platform for wavelength-dependent optoelectronic sensing and signal classification systems.

1 | Introduction

A wavelength-selective and dual-mode photoresponse photodetector is critical for the emerging technology of imaging, optical communication, environmental monitoring, and advanced optoelectronic sensing [1–4]. In particular, the ability to intrinsically distinguish incident wavelengths at the device level is highly desirable for multifunctional and integrated optoelectronic systems [5–9]. However, conventional photodetectors based on photovoltaic or photoconductive effects typically lack intrinsic wavelength discrimination and often require external optical filters or complex signal processing to achieve spectral selectivity [10–14]. Consequently, there is an urgent need to develop photodetectors that can effectively integrate multiple photoresponse

Jiaqi Tang and Dongdong Zhao contributed equally to this work.

All rights reserved, including rights for text and data mining and training of artificial intelligence technologies or similar technologies.
© 2026 Wiley-VCH GmbH

mechanisms within a single platform to achieve wavelength-dependent signal differentiation [15].

Two-dimensional (2D) transition metal dichalcogenides (TMDs), such as MoS_2, offer remarkable advantages including atomic thickness and tunable bandgaps across the visible-near-infrared range, making them ideal channels for miniaturized and high-performance optoelectronic devices [16–19]. However, their inherently weak optical absorption limits their photoresponse efficiency. To address this limitation, integrating 2D semiconductors with strongly absorptive materials has emerged as an effective strategy to modify light–matter interaction and introduce additional interfacial response pathways [20–22]. Owing to their atomically flat and dangling-bond-free surfaces, TMDs can readily form van der Waals (vdW) heterostructures with diverse materials without lattice-matching constraints, providing a versatile platform for constructing hybrid systems with complementary functionalities and synergistic photoresponses [23]. Recent studies have demonstrated that such hybrid structures can significantly enhance light absorption and carrier separation. Nevertheless, these devices are still largely dominated by steady-state photoconductive responses and lack intrinsic wavelength-selective functionality [20, 24].

Hybrid halide perovskites (e.g., $MAPbBr_3$) have recently emerged as outstanding partners for constructing such hybrid systems due to their strong light absorption, long carrier diffusion lengths, and potential thermally induced transient electrical response under optical excitation [25–27]. Beyond conventional photocarrier generation, recent studies have suggested that photothermal effects induced by light absorption may lead to transient electrical responses associated with lattice dynamics or interfacial processes [28–30]. However, in most reported TMDs/perovskite heterostructures, the photoresponse is still dominated by steady-state photoconductivity, while wavelength-dependent transient behaviors arising from interfacial thermal effects remain largely unexplored [31–33]. This is partly due to the complexity of interface energetics and the instability of perovskite materials under illumination or bias [30, 34]. As a result, achieving intrinsic wavelength-dependent signal differentiation within a single device architecture remains a challenge.

Here, we present a $MoS_2/MAPbBr_3$ heterojunction photodetector, which exhibits dual-mode light response. Utilizing this dual-mode response, this device can be applied to the classification of structured red–green optical signals through a simple classification algorithm. Specifically, green light excitation generates a stable photoconductive current related to the generation and transport of charge carriers in the device, while red light illumination generates a transient thermally-driven current, which is due to thermally induced interfacial modulation. This wavelength-dependent response enables direct electrical discrimination between different optical inputs. This discrimination arises from the different excitation conditions relative to the $MAPbBr_3$ bandgap, which lead to distinct response mechanisms and temporal characteristics. As a proof-of-concept, the device is further employed for the recognition of structured red–green optical signals using a simple classification algorithm. This work addresses the challenge of wavelength-dependent signal differentiation by introducing a dual-mode response mechanism based on photoconductive and thermally induced interfacial effects within a single device architecture. Unlike conventional broadband photodetectors, this work focuses on wavelength-dependent signal encoding enabled by coupled physical mechanisms. This result represents a proof-of-concept demonstration based on discrete excitation conditions relative to the $MAPbBr_3$ bandgap, rather than a general color recognition mechanism across the full visible spectrum.

2 | Results and Discussion

To illustrate conceptually the wavelength-dependent recognition capability of our device, a real traffic light lighting scenario is shown in Figure 1a as the external optical input. The corresponding device structure and electrical output states under red and green light irradiation are shown in Figure 1b, demonstrating how the $MoS_2/MAPbBr_3$ heterostructure converts different light stimuli into distinguishable electrical signals.

To verify the dual-mode optical detection mechanism of photodetectors and thermosensitive detectors, we constructed an optical detector based on a large-area $MoS_2/MAPbBr_3$ heterojunction. The detailed manufacturing process is shown in Figures S1 and S2 presents representative optical microscope images corresponding to the key manufacturing steps, confirming the relative positions of the materials and the clear geometries of the devices. In this structure, the continuous MoS_2 is in direct contact with the Au electrode, while the $MAPbBr_3$ perovskite layer is deposited on top of the MoS_2 through a spraying process. This vertical van der Waals heterostructure provides a $MoS_2/MAPbBr_3$ contact region for interfacial charge and heat coupling while retaining a lateral MoS_2 transport pathway.

Under green-light illumination (520 nm), the $MAPbBr_3$ layer serves as the primary light absorber, generating abundant photocarriers. Due to the favorable type-II band alignment at the $MoS_2/MAPbBr_3$ interface, photogenerated electrons are efficiently transferred from the conduction band of $MAPbBr_3$ to MoS_2, while holes remain in the perovskite layer. The transferred electrons are then transported through the lateral MoS_2 channel, resulting in a stable photoconductive current [35, 36]. On the contrary, red-light excitation induces thermally driven interfacial modulation at the $MoS_2/MAPbBr_3$ heterointerface, producing a transient current response associated with thermally induced interfacial modulation. These different responses to different wavelengths of light allow the device to distinguish between the colors of illumination. This behavior enables the device to generate distinguishable electrical signals corresponding to different optical inputs.

A continuous 2-inch single-layer MoS_2 film was successfully synthesized by the chemical vapor deposition (CVD) method (Figure 1c). During the growth process, MoO_3 and sulfur powder were used as precursors in a spatially separated configuration. Eventually, individual MoS_2 domains seamlessly merged to form a continuous film of uniform thickness across the entire substrate (see Supporting Information). Optical microscope images from multiple regions of the wafer (Figure S3) confirm the continuous wafer-scale coverage of the MoS_2 film. To further evaluate the spatial uniformity, large-area Raman mapping of the E^1_{2g} mode was performed at representative regions of the MoS_2 film

16163028, 2026, 71, Downloaded from https://advanced.onlinelibrary.wiley.com/doi/10.1002/adfm.77559 by Beihang University (Buaa), Wiley Online Library on [23/09/2026]. See the Terms and Conditions (https://onlinelibrary.wiley.com/terms-and-conditions) on Wiley Online Library for rules of use; OA articles are governed by the applicable Creative Commons License

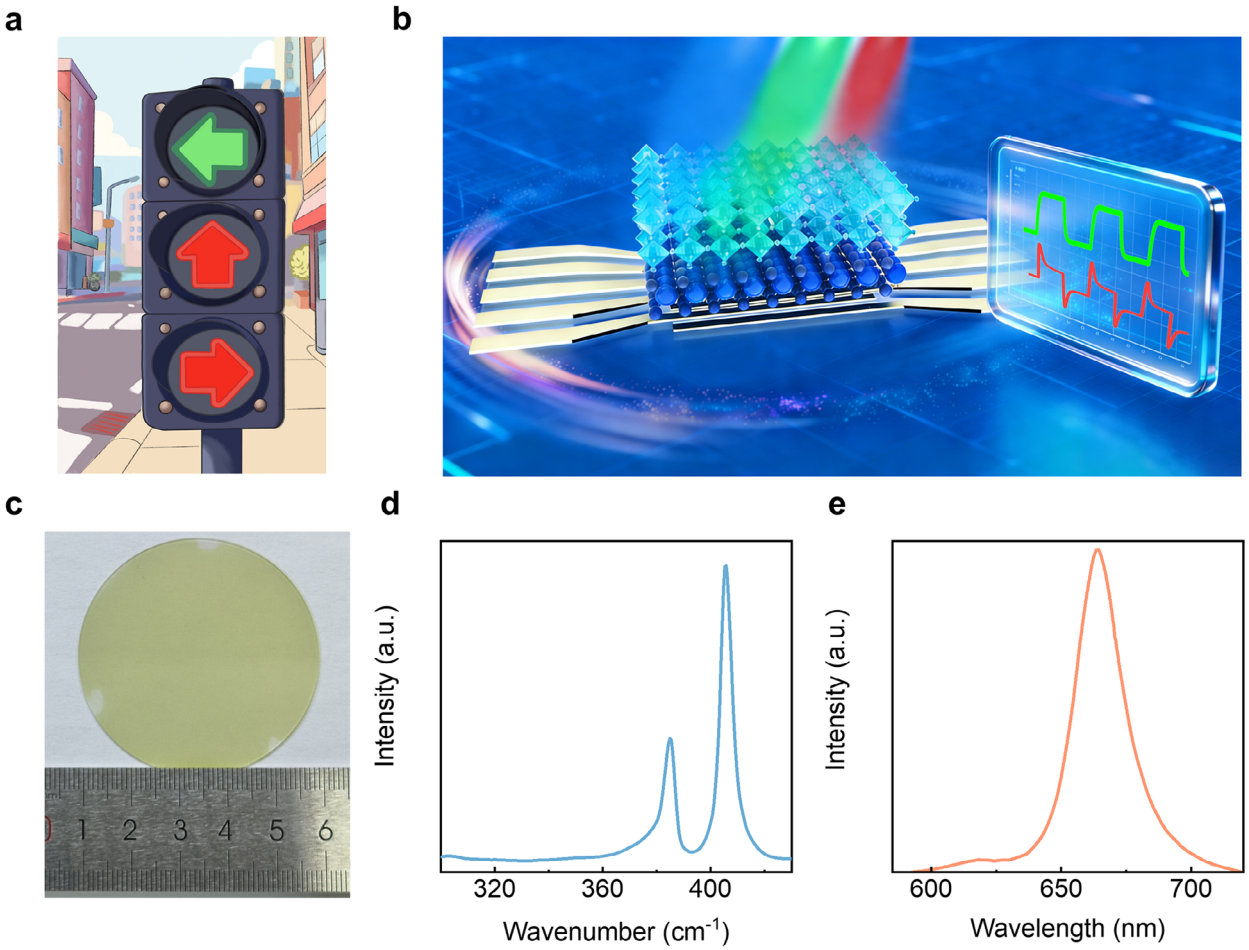


FIGURE 1 | Simulated red/green input signals and MoS_2-based device characterization. (a) Schematic illustration of a traffic signal light representing red and green illumination inputs. (b) Schematic illustration of the MoS_2-based device structure and the corresponding output signal states. (c) Optical photograph of the wafer-scale MoS_2 film, demonstrating high uniformity. (d) Raman spectrum of MoS_2 with characteristic peaks. (e) Photoluminescence (PL) spectrum of MoS_2, confirming its direct-bandgap nature and material quality.

(Figure S4a). The E^1_{2g} Raman mapping shows a relatively uniform intensity distribution over the mapped areas, supporting the structural consistency of the CVD-grown MoS_2 film. In addition, Raman line-scan measurements were conducted as a long-range check of Raman signal consistency across the sample, where the characteristic E^1_{2g} and A_{1g} modes remain clearly resolved along the scan direction (Figure S4b). Raman and photoluminescence (PL) spectra confirm the monolayer nature of the film, with characteristic E^1_{2g} and A_{1g} Raman peaks located at ~384 and ~404 cm^{-1} and a distinct PL emission peak around 1.83 eV (Figure 1d,e).

These features indicate good thickness uniformity across the wafer. The continuously defect-minimized morphology of the CVD-grown film offers an ideal substrate for constructing large-area vdW heterojunctions with perovskite layers. In comparison to isolated domain-based structures, there is the uniformity of interfacial coupling and electronic properties, which is advantageous for stable and reproducible photoresponse on the wafer scale [34–37]. Consequently, the MoS_2 films offer a potential route for developing hybrid photodetectors with enhanced functionality.

2.1 | Photoconductive Response of Monolayer MoS_2

Before constructing the heterojunction, a systematic study was conducted on the photoconductivity performance of the grown single-layer MoS_2. The transfer characteristics of a representative top-gated MoS_2 device were measured to evaluate the basic electrical behavior of the MoS_2 channel (Figure S5). The I_{ds}–V_{gs} curves show clear gate-modulated semiconducting transport behavior, supporting the role of MoS_2 as a lateral transport channel in the device. A large-area MoS_2 film was transferred onto the pre-prepared crossed electrodes to fabricate a planar photodetector, as shown in Figure 2a. The continuous morphology between MoS_2 and the electrodes is beneficial for carrier transport, as they help reduce interface scattering and contact resistance [37, 38].

The current-voltage (I–V) characteristics under dark conditions and at different light intensities were measured to evaluate the light response behavior. As shown in Figure 2b,c, whether it is red ($\lambda = 650$ nm) or green ($\lambda = 520$ nm) light, it causes a slight increase in current compared to the dark state, which is consistent with the photoconductive response. However, the overall enhancement of

16163028, 2026, 71, Downloaded from https://advanced.onlinelibrary.wiley.com/doi/10.1002/adfm.77559 by Beihang University (Buaa), Wiley Online Library on [23/09/2026]. See the Terms and Conditions (https://onlinelibrary.wiley.com/terms-and-conditions) on Wiley Online Library for rules of use; OA articles are governed by the applicable Creative Commons License

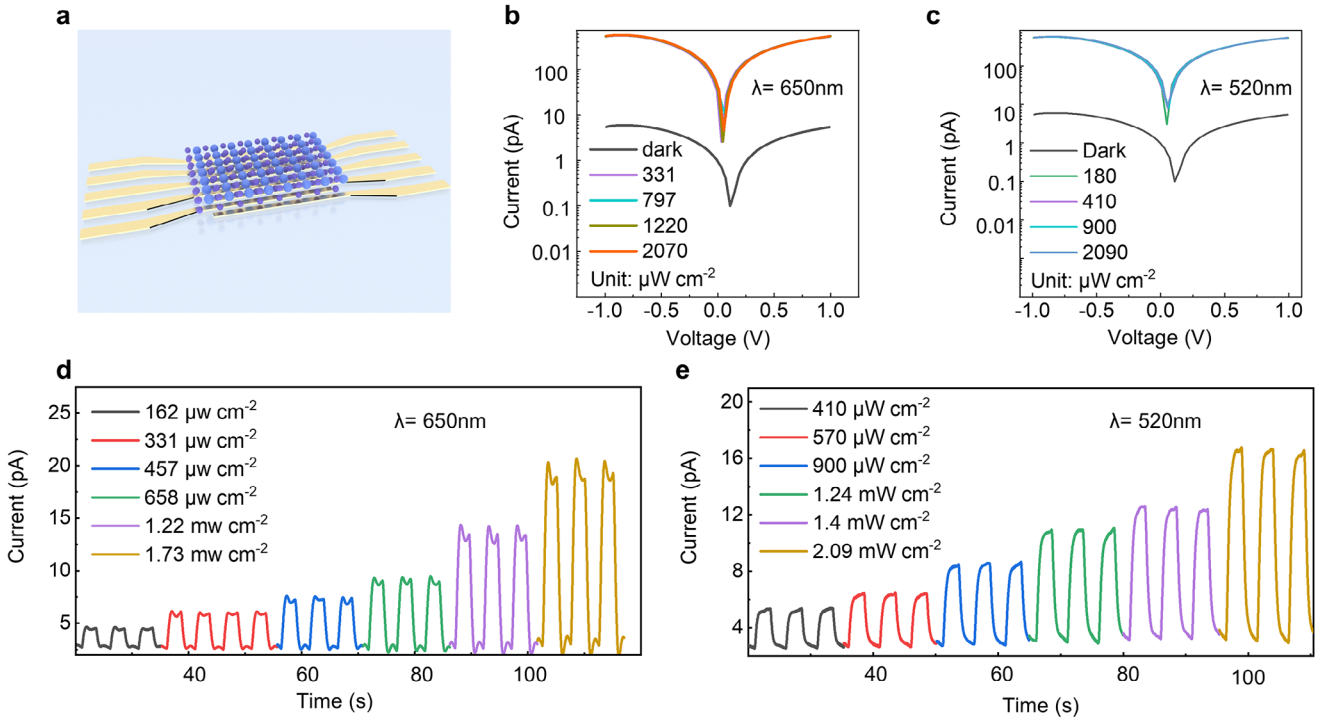


FIGURE 2 | Photoconductive response of wafer-scale monolayer MoS_2. (a) Schematic illustration of the photodetector structure based on continuous monolayer MoS_2. (b) Current-voltage (*I–V*) characteristics of the MoS_2 device under red-light illumination (650 nm) with varying optical power, showing a modest photocurrent enhancement. (c) IV curves under green-light illumination (520 nm) with different power intensities, demonstrating slightly stronger photoconductive behavior compared with the red-light condition. (d) Time-resolved photocurrent (*I–t*) traces acquired under red-light excitation at multiple powers, showing stable but weak photocurrent switching. (e) *I–t* response under green-light illumination at different powers, revealing a reproducible and persistent photoconductive plateau. These results confirm that monolayer MoS_2 exhibits intrinsic photoconduction for both wavelengths, although the photocurrent amplitude remains limited due to low absorption cross-section of the ultrathin film. Photocurrent response measured at $V_{ds} = 1$ V under 520 nm illumination. Time-resolved photocurrent measured at $V_{ds} = 1$ V under 650 nm illumination with different incident power densities.

the photocurrent is relatively limited, and its dependence on the incident light power is weak. This can be attributed to the limited optical absorption of the atomic-thin MoS_2.

Time-resolved photocurrent (*I–t*) measurements (Figure 2d,e) further demonstrated that under periodic illumination conditions, the on/off switching behavior was stable and repeatable. Notably, the temporal responses under 520 and 650 nm illumination exhibit distinct characteristics. Under 520 nm illumination, the photon energy is well above the bandgap of MoS_2, leading to efficient photocarrier generation. As a result, the photocurrent shows a monotonic rise and decay behavior dominated by carrier generation and transport processes. In contrast, under 650 nm illumination, the absorption in MoS_2 is significantly weaker, resulting in a lower photocarrier density. In this regime, the photocurrent becomes more sensitive to carrier trapping and detrapping processes. Upon illumination, photocarriers are initially generated, leading to a rapid increase in current, followed by a slight decrease as trapping and recombination processes become dominant before reaching steady state. These processes occur on different time scales, giving rise to the observed non-monotonic temporal feature. However, regardless of whether it was stimulated by red light or green light, the amplitude of the photocurrent was relatively small. These observations confirmed that although molybdenum disulfide is photo-sensitive, its photoconductivity efficiency is fundamentally limited by its limited light-matter interaction. It should be noted that this weak non-monotonic behavior is fundamentally different from the pronounced transient response observed in the $MoS_2/MAPbBr_3$ heterostructure, where the signal is dominated by interfacial coupling effects. Therefore, coupling monolayer MoS_2 with a strongly absorbing perovskite layer provides a route to introduce additional interfacial response channels beyond the weak intrinsic photoconductive response of MoS_2.

2.2 | Dual-Mode Photoresponse in $MoS_2/MAPbBr_3$ Heterojunction Photodetectors

To enhance the light-material interaction and achieve dual-modal light response, a hybrid light detector was fabricated by spraying a $MAPbBr_3$ perovskite layer onto a wafer-level monolayer MoS_2 film (Figure 3a). The perovskite layer was prepared through a controllable spray coating process, followed by a mild thermal annealing treatment to promote crystallization, and enhance interfacial adhesion. The surface coverage area was intentionally designed to be smaller than the MoS_2 channel region, providing both a direct MoS_2 conduction path and a $MoS_2/MAPbBr_3$ contact region for interfacial charge and heat coupling (Figure S6). Optical microscopy confirms that the spray-coated $MAPbBr_3$ layer is mainly confined within the MoS_2 channel region, while SEM

16163028, 2026, 71, Downloaded from https://advanced.onlinelibrary.wiley.com/doi/10.1002/adfm.77559 by Beihang University (Buaa), Wiley Online Library on [23/09/2026]. See the Terms and Conditions (https://onlinelibrary.wiley.com/terms-and-conditions) on Wiley Online Library for rules of use; OA articles are governed by the applicable Creative Commons License

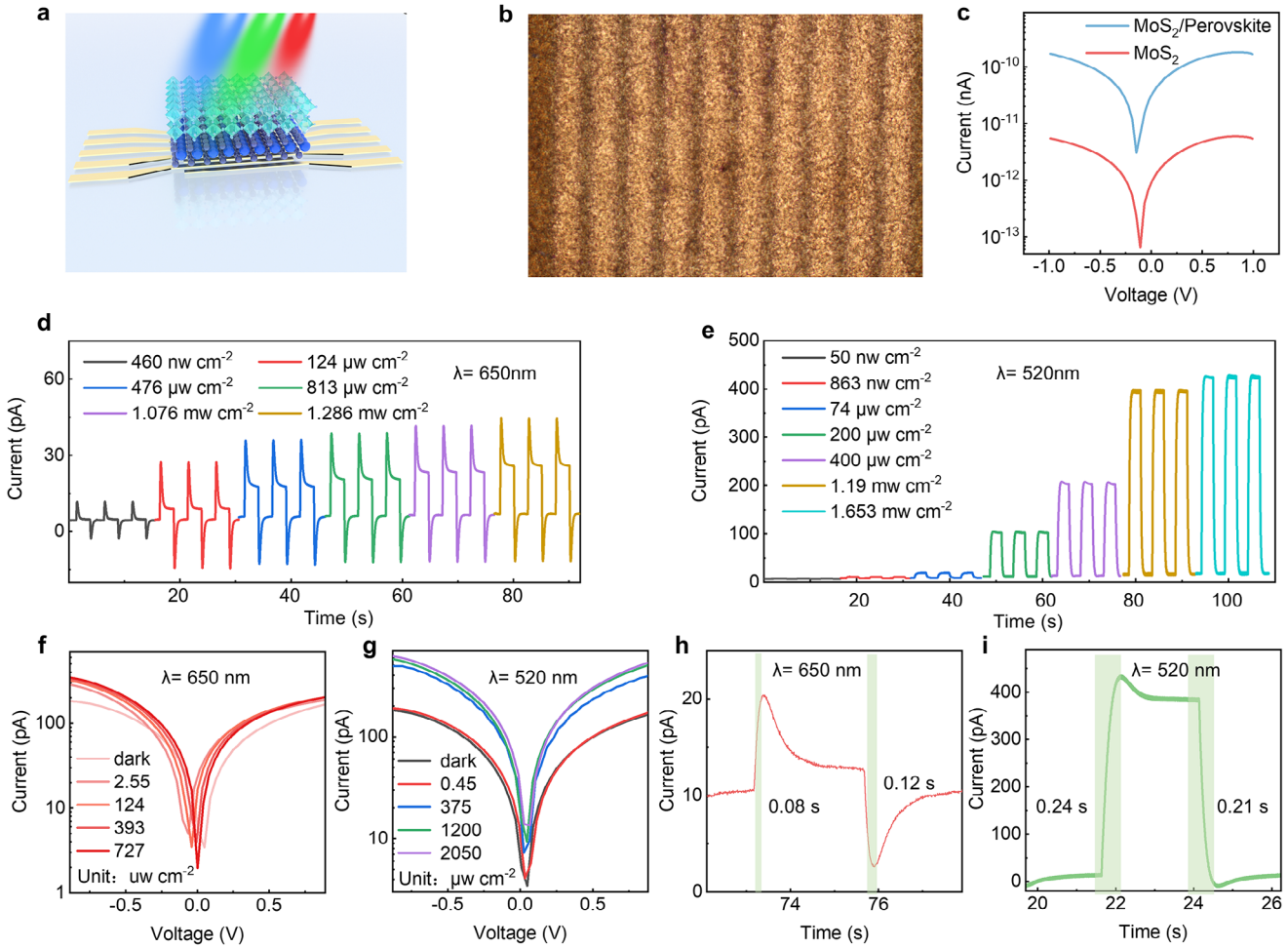


FIGURE 3 | Dual-mode photoresponse of MoS_2/$MAPbBr_3$ hybrid photodetectors. (a) Schematic illustration of the hybrid device structure with partial $MAPbBr_3$ coverage on the monolayer MoS_2 channel. (b) Scanning electron microscopy (SEM) image showing the morphology of $MAPbBr_3$. (c) Comparison of dark current between MoS_2/$MAPbBr_3$ hybrid device and pristine MoS_2 channel, showing slightly enhanced baseline current due to interfacial coupling and additional carrier transport pathways. (d) *I*–*t* response under red-light illumination, exhibiting transient current spikes originating from thermally driven interfacial modulation MoS_2/$MAPbBr_3$ heterointerface. (e) *I*–*t* response under green-light excitation, demonstrating a stable photoconductive dominated by photon-induced carrier transport. (f) Red-light IV characteristics at different illumination powers, showing negligible steady-state current variation. (g) Green-light IV characteristics at varying powers, exhibiting monotonic photocurrent increase characteristic of photoconductive behavior. (h) Temporal response of the thermally induced red-light channel, showing rapid rise and decay dynamics. (i) Temporal response of the photoconductive green-light channel, with slightly slower but stable kinetic behavior. These measurements collectively confirm that the hybrid heterojunction enables distinguishable dual-mode photodetection, arising from coupled photoconductive and thermally induced interfacial effects mechanisms. Photocurrent response measured at $V_{ds} = 1$ V under 520 nm illumination. Time-resolved photocurrent measured at $V_{ds} = 1$ V under 650 nm illumination with different incident power densities.

characterization reveals a granular $MAPbBr_3$ morphology in the selected coated region (Figure 3b and Figures S6 and S7). To further verify the functional MoS_2/$MAPbBr_3$ contact region, atomic force microscopy (AFM) characterization was performed across the edge of the spray-coated $MAPbBr_3$ region to confirm the vertical stacking and height step at the MoS_2/$MAPbBr_3$ boundary (Figure S8). The height profile reveals a step of ~0.46 μm, corresponding to the $MAPbBr_3$ layer on MoS_2. Because this region is located near the coating edge, partially discontinuous or island-like $MAPbBr_3$ features are observed at the boundary, which are attributed to the spray-coating process and mask-defined edge effect. Nevertheless, the observed spatial overlap between $MAPbBr_3$ and MoS_2 supports the formation of a functional MoS_2/$MAPbBr_3$ contact region.

Quantitative analysis of the photoconductive response under 520 nm illumination is provided in Figure S9. The photocurrent follows a power-law dependence on illumination intensity ($I_{ph} \propto P^{\alpha}$, $\alpha = 0.68$), while the responsivity decreases with increasing power density, consistent with typical photoconductive behavior.

The hybrid device exhibits a slightly higher dark current compared to pristine MoS_2 (Figure 3c). The dark current is on the order of 167 pA at a bias of 1 V, as extracted from the *I*–*V* characteristics. The baseline current in the *I*–*t* measurements remains stable under dark conditions, indicating reliable device operation. The *I*–*t* curve under red light excitation (λ = 650 nm) shows transient current peaks, which rapidly decay to the baseline once the light is turned off (Figure 3d). Although the optical absorption

16163028, 2026, 71, Downloaded from https://advanced.onlinelibrary.wiley.com/doi/10.1002/adfm.77559 by Beihang University (Buaa), Wiley Online Library on [23/09/2026]. See the Terms and Conditions (https://onlinelibrary.wiley.com/terms-and-conditions) on Wiley Online Library for rules of use; OA articles are governed by the applicable Creative Commons License

of monolayer MoS_2 is limited [39], non-radiative relaxation of photoexcited carriers can efficiently generate localized heating at the nanoscale, as reported in previous studies [28, 29]. This process does not involve macroscopic temperature increase, but rather local thermal modulation at the $MoS_2/MAPbBr_3$ interface. This transient behavior originates from thermally induced interfacial modulation at the $MoS_2/MAPbBr_3$ junction. The temperature variation induces modulation of the interfacial potential, resulting in transient current signals.

Unlike red light illumination, under green light illumination (λ = 520 nm), the *I–t* curves show a stable and repeatable photogenerated current plateau (Figure 3e), corresponding to photoconductivity. At this wavelength, the $MAPbBr_3$ layer exhibits strong optical absorption, leading to efficient photocarrier generation. Under 520 nm illumination, photocarriers are generated in the $MoS_2/MAPbBr_3$ heterostructure, predominantly in the $MAPbBr_3$ layer owing to its strong above-bandgap absorption. Based on the reported type-II band alignment of MoS_2/perovskite heterostructures, electrons are expected to transfer or accumulate toward the MoS_2 channel, while holes are retained or accumulated in the $MAPbBr_3$ layer. This spatial charge separation, together with lateral carrier transport through the MoS_2 channel, contributes to the steady-state photoconductive current [40, 41]. As a result, the total steady-state photocurrent achieves a sum of the contributions from both layers, with the perovskite layer absorbing the photons and generating the carriers and the MoS_2 channel facilitating lateral carrier transport.

The corresponding *I–V* characteristics further support these observations. To quantitatively evaluate the photoconductive performance, the responsivity (R) was calculated using $R = I_{ph} / (P \times A)$, where I_{ph} is the photocurrent, P is the incident power density, and A is the effective device area. Under 520 nm illumination, the responsivity extracted from the steady-state photocurrent ranges from $\sim 8.4 \times 10^{-5}$ to $\sim 9.8 \times 10^{-4}$ A W^{-1}, depending on the illumination power density. The responsivity decreases with increasing power density, which is attributed to trap-state saturation and enhanced carrier recombination at higher excitation levels. When the red-light power is increased (Figure 3f), the steady-state *I–V* curve only shows a weak power dependence, indicating that the response induced by red light is not a conventional photoconduction. While under green light illumination (Figure 3g), the photocurrent monotonically increases with the illumination power, which is consistent with the typical power-dependent photoconductive behavior.

Time-resolved measurements (Figure 3h,i) further reveal distinct dynamic features for the two response modes. Under red-light illumination, the response shows a faster rise and decay (~0.08/0.12 s), which is attributed to thermally induced interfacial modulation involving heat generation, thermal diffusion, and subsequent relaxation processes. For red-light excitation (650 nm), the response is dominated by transient current rather than steady-state photoconduction. Therefore, a conventional responsivity definition is not strictly applicable, and the peak transient current is used to characterize the response amplitude. The red-light response is governed by localized photothermal effects in the MoS_2 layer and subsequent interfacial modulation. Photothermal responses in MoS_2-based systems have been widely reported and are strongly influenced by interfacial thermal transport properties [42]. Therefore, the observed response time (10^{-2}–10^{-1} s) is physically consistent with thermally induced interfacial processes involving heat generation, diffusion, and relaxation at the heterointerface. Under green-light illumination, the response exhibits slightly slower but more stable dynamics (~0.24/0.21 s), governed by carrier generation, transport, and recombination processes. Under green-light illumination, the response is dominated by photoconductive processes due to efficient carrier generation, which determines the overall temporal behavior of the device. Consistent behavior is also observed under 460 nm illumination, further confirming that the response mechanism depends on whether the excitation energy is above or below the $MAPbBr_3$ bandgap (Figure S10). The difference in temporal behavior originates from the distinct underlying mechanisms: thermally driven interfacial effects under red-light excitation vs. photoconductive carrier dynamics under green-light illumination. This separation of time-domain signatures enables reliable discrimination between different optical inputs based on their temporal current responses.

The responsivity obtained in this work is lower than that of high-gain MoS_2 phototransistors reported in the literature. For example, mechanically exfoliated monolayer MoS_2 phototransistors can exhibit responsivity up to 880 A W^{-1}, while mechanically exfoliated multilayer MoS_2 phototransistors integrated with charge-trapping HfO_2 dielectrics can reach values as high as 1.1×10^6 A W^{-1} due to strong photogating gain [41, 42]. Other engineered MoS_2-based photodetectors also show responsivity values spanning several orders of magnitude depending on device architecture, photogain mechanism, and measurement conditions [43, 44]. In contrast, the present device does not employ gate-assisted photogating, charge-trapping dielectric amplification, or optimized contact engineering to maximize responsivity. Its relatively low responsivity is likely related to the absence of gain-enhancing mechanisms, the large effective illuminated area used in the calculation, the limited optical absorption of monolayer MoS_2, and possible recombination/trapping at the spray-coated $MoS_2/MAPbBr_3$ interface. Therefore, the present work should not be regarded as a high-responsivity photodetector demonstration, but rather as a proof-of-concept device that uses a hybrid heterointerface to generate two temporally distinct photoresponse modes. Importantly, the red-light transient response does not originate from intrinsic polarization in $MAPbBr_3$, but from thermally induced modulation of the interfacial electronic structure [45]. The observed wavelength-dependent response arises from the change in the dominant contribution to the total current under different excitation conditions. This demonstration is limited to discrete excitation conditions (e.g., red and green) and does not represent general color recognition under mixed spectral inputs.

To evaluate the stability of the transient response under repeated thermal cycling, cyclic *I–t* measurements were performed under periodic 650 nm illumination (Figure S11). The transient current peaks remain stable over 1 h, with negligible variation in peak amplitude and waveform. This indicates that the thermally induced interfacial response is reproducible under repeated light-induced heating and cooling processes. The observed stability suggests that the temperature variation involved is localized and moderate, and does not lead to noticeable degradation of the $MoS_2/MAPbBr_3$ interface within the tested conditions. To

16163028, 2026, 71, Downloaded from https://advanced.onlinelibrary.wiley.com/doi/10.1002/adfm.77559 by Beihang University (Buaa), Wiley Online Library on [23/09/2026]. See the Terms and Conditions (https://onlinelibrary.wiley.com/terms-and-conditions) on Wiley Online Library for rules of use; OA articles are governed by the applicable Creative Commons License

further evaluate device-to-device reproducibility, photoresponse measurements were performed on multiple MoS_2/$MAPbBr_3$ heterostructure devices under the same measurement conditions (Figure S12). The measured devices exhibit consistent wavelength-dependent response modes, with steady-state photocurrent under 520 nm illumination and transient current peaks under 650 nm illumination. Although variations in the absolute current amplitude are observed, likely due to local differences in the spray-coated $MAPbBr_3$ coverage, perovskite thickness, and interfacial contact quality, the characteristic dual-mode response is reproducibly observed across the measured devices. Further optimization of the $MAPbBr_3$ deposition process and interfacial morphology will be important for improving responsivity, spatial uniformity, and device-to-device reproducibility.

Through the coupling between optical excitation and thermally induced interfacial effects, a dual-mode photoresponse is achieved within a single device, enabling wavelength-dependent signal differentiation. The continuous MoS_2 film provides a scalable material platform for constructing MoS_2/$MAPbBr_3$ heterostructure photodetectors.

2.3 | Mechanism Discussion

Under red light excitation, the hybrid MoS_2/$MAPbBr_3$ photodetector exhibits a characteristic four-stage transient photocurrent evolution, indicating a thermally induced interfacial transient mechanism (Figure 4a). The detailed process is shown in Figure 4b. Under red-light excitation (λ = 650 nm), the photon energy is below the bandgap of $MAPbBr_3$, and thus direct photocarrier generation in the perovskite is negligible. Instead, partial absorption in the MoS_2 layer leads to localized heating at the MoS_2/$MAPbBr_3$ interface. Such thermal transfer is feasible given that thermal boundary conductance across van der Waals interfaces is typically on the order of 10^6–10^7 W m^{-2} K^{-1} [46, 47]. This localized temperature variation at the MoS_2/$MAPbBr_3$ interface induces modulation of the interfacial potential and carrier distribution. Importantly, this transient response is attributed to thermally induced interfacial effects rather than intrinsic pyroelectricity of $MAPbBr_3$, and is enabled by the strong coupling between thermal dynamics and charge transport at the heterointerface.

At the initial stage (Stage I), the rapid temperature increase induces a sudden modulation of the interfacial potential, resulting in a transient current peak. As illumination continues (Stage II), the system reaches thermal equilibrium, and the transient contribution diminishes, leaving a low steady-state current. When the light is turned off (Stage III), the rapid cooling process induces an opposite transient response due to the relaxation of the interfacial potential. Finally (Stage IV), the current returns to the baseline as thermal equilibrium is restored.

This bidirectional transient behavior confirms that the red-light response originates from the thermally induced interfacial modulation triggered by the absorption of MoS_2 and interface heat transfer, rather than from the direct generation of photogenerated carriers in $MAPbBr_3$. The interfacial coupling between MoS_2 and $MAPbBr_3$ allows thermally induced changes in the interfacial potential to modulate the charge distribution in the MoS_2 channel. This process gives rise to a transient response distinct from the steady-state photoconductive response observed under green-light excitation.

To confirm that the observed thermally induced transient behavior originates from interface coupling rather than the intrinsic properties of $MAPbBr_3$, a comparative experiment was conducted on the original perovskite film. As shown in Figure S13, the original $MAPbBr_3$ device exhibited a significant photoconductive response under green light irradiation, while it showed almost no response under high-power red-light excitation. The direct comparison under the same illumination power further emphasized that the transient red-light response was only observed in the MoS_2/$MAPbBr_3$ heterojunction, but not in a single material (Figure S14). These results support that the transient response originates from the synergistic interaction between MoS_2 absorption and thermally induced interfacial modulation.

The MoS_2/$MAPbBr_3$ heterostructure is expected to form a type-II band alignment, where the conduction band minimum of MoS_2 lies below that of $MAPbBr_3$, facilitating electron transfer from the perovskite layer to MoS_2, while holes remain in $MAPbBr_3$ [32, 40]. To provide additional experimental support for the interfacial potential distribution, KPFM measurements were performed across the MoS_2/$MAPbBr_3$ heterointerface using a Pt-coated conductive probe (Figure S15). A clear surface-potential contrast is observed between the MoS_2 and $MAPbBr_3$ regions. The line profile shows that the measured potential decreases from the MoS_2 region to the $MAPbBr_3$ region, with a potential difference of approximately 70–90 mV. This result indicates the presence of an interfacial potential gradient and supports electronic coupling at the MoS_2/$MAPbBr_3$ heterointerface. Because the Pt-probe work function was not independently calibrated with a standard reference sample, the KPFM result is used here to compare relative surface-potential differences rather than to extract absolute work-function values. Based on these observations, the schematic band diagrams of the MoS_2/$MAPbBr_3$ heterojunctions under red and green light irradiation (Figure 4c,d) further analyzed the different physical origins of the light response. Under red light excitation (Figure 4c), the photon energy (~1.65 eV) is lower than the bandgap of $MAPbBr_3$ (~2.3 eV), and thus direct photocarrier generation in the perovskite is negligible. In this case, light is weakly absorbed by the MoS_2 layer, and the absorbed energy is primarily converted into localized heat through non-radiative relaxation, leading to a temperature increase near the interface. This temperature variation modulates the interfacial electronic structure and carrier distribution, resulting in transient charge redistribution at the interface. It should be emphasized that the red-light response is not attributed to selective photocarrier transfer from $MAPbBr_3$ to MoS_2, because direct photocarrier generation in $MAPbBr_3$ is negligible under sub-bandgap excitation. Therefore, the device exhibits two distinct response mechanisms: thermally induced interfacial modulation under red-light excitation and photoconductive carrier transport under green-light illumination. The red-light response is primarily governed by interface heat transfer and interfacial potential modulation.

In contrast, under green light illumination (Figure 4d), the photon energy (~2.3 eV) exceeds the bandgap of $MAPbBr_3$, enabling efficient photocarrier generation in the perovskite layer

16163028, 2026, 71, Downloaded from https://advanced.onlinelibrary.wiley.com/doi/10.1002/adfm.77559 by Beihang University (Buaa), Wiley Online Library on [23/09/2026]. See the Terms and Conditions (https://onlinelibrary.wiley.com/terms-and-conditions) on Wiley Online Library for rules of use; OA articles are governed by the applicable Creative Commons License

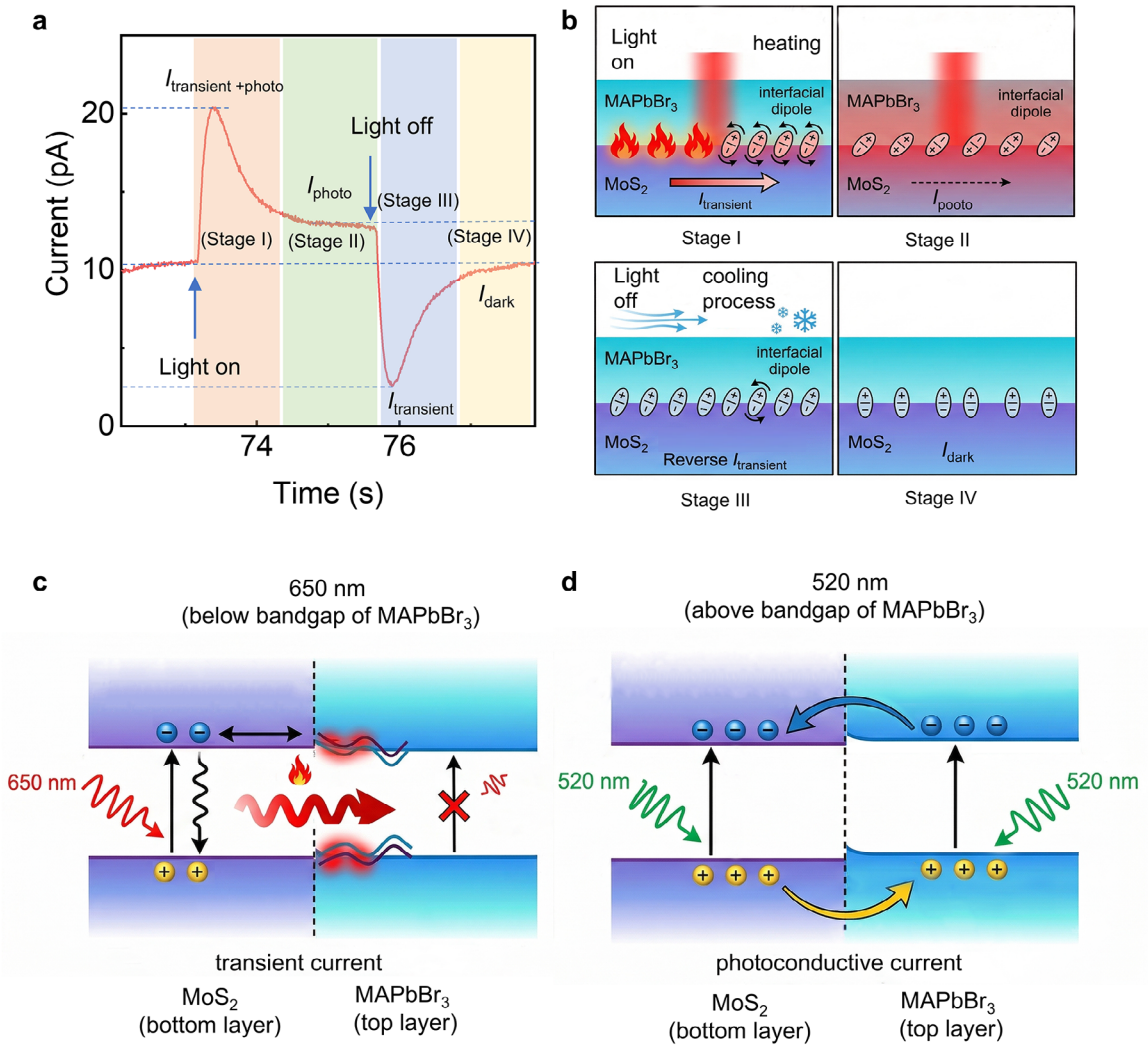


FIGURE 4 | Mechanistic illustration of wavelength-dependent photoresponse in $MoS_2/MAPbBr_3$ heterojunction. (a) Transient photocurrent behavior under red-light excitation, exhibiting a four-stage evolution characteristic of a thermally induced response. (b) Thermally induced transient response mechanism based on interfacial thermal modulation. (c) Energy band alignment and carrier dynamics under red-light illumination. (d) Energy band alignment and carrier-separation process under 520 nm illumination. Above-bandgap excitation generates photocarriers in the $MoS_2/MAPbBr_3$ heterostructure, predominantly in $MAPbBr_3$. Driven by the type-II band alignment, electrons transfer or accumulate toward MoS_2, while holes are retained or accumulated in $MAPbBr_3$, resulting in spatial charge separation and steady-state photoconductive transport through the MoS_2 channel. These distinct pathways illustrate that the red- and green-light responses arise from different dominant mechanisms: thermally induced interfacial potential modulation under red-light excitation and type-II-band-alignment-assisted photoconduction under green-light illumination.

[48, 49]. Although MoS_2 may also absorb light, its contribution is relatively weak. Driven by the type-II band alignment, photogenerated electrons are transferred from $MAPbBr_3$ to MoS_2, while holes remain in the perovskite layer, leading to efficient charge separation and sustained photocurrent generation [32, 50]. This process is dominated by direct photogenerated carrier transfer rather than thermal or polarization effects.

As a result, the two excitation conditions activate different dominant pathways: red-light excitation induces thermally driven interfacial potential modulation, whereas green-light excitation induces type-II-band-alignment-assisted carrier separation and steady-state photoconductive transport. This simultaneous mechanism and tunability show the exceptional multifunctional coupling of the $MoS_2/MAPbBr_3$ heterostructure in wavelength-dependent photoresponse behaviors. MoS_2 serves as a lateral transport channel and provides favorable energy-level alignment with $MAPbBr_3$, facilitating charge separation and carrier transport in the heterostructure [41].

2.4 | Wavelength-Encoded Optical Signal Classification

To evaluate the potential of the proposed photodetector for optical signal recognition, the wavelength-dependent dual-mode photoresponse was integrated into a data-driven perception framework inspired by traffic signal recognition. In this scheme, optical information is encoded simultaneously by illumination color and spatial distribution, analogous to real-world traffic lights conveying semantic cues through both chromatic and geometric features (Figure 5a).

16163028, 2026, 71, Downloaded from https://advanced.onlinelibrary.wiley.com/doi/10.1002/adfm.77559 by Beihang University (Buaa), Wiley Online Library on [23/09/2026]. See the Terms and Conditions (https://onlinelibrary.wiley.com/terms-and-conditions) on Wiley Online Library for rules of use; OA articles are governed by the applicable Creative Commons License

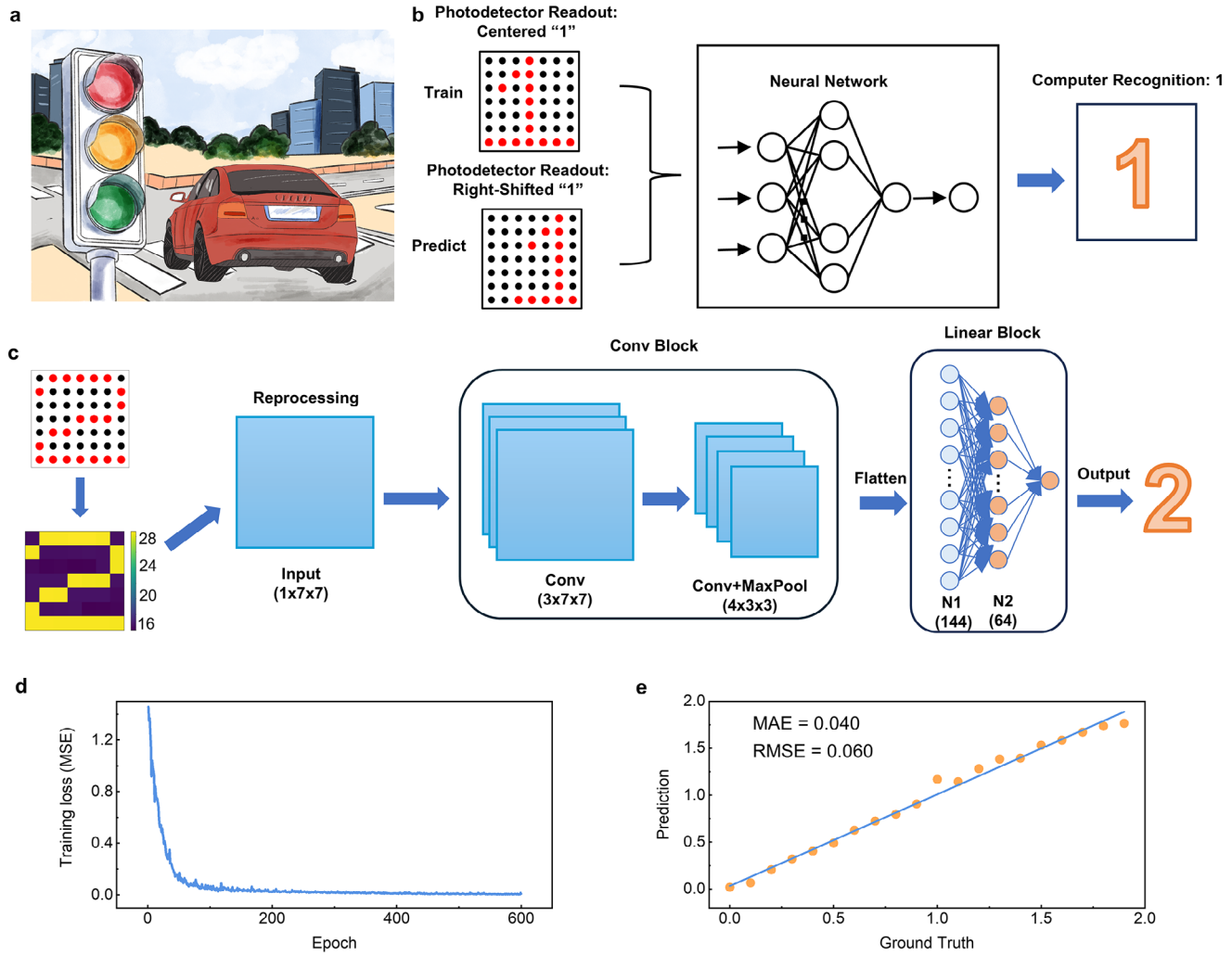


FIGURE 5 | Optical signal recognition based on photodetector readouts. (a) Schematic illustration of traffic-signal-inspired optical inputs used for recognition tasks. (b) Training and testing strategy using 7 × 7 photodetector readouts. Centered digit patterns are used for training, while right-shifted patterns are employed for testing to evaluate model generalization under spatial misalignment. (c) Overview of the neural network architecture, including learnable preprocessing, convolutional feature extraction, and linear output layers. (d) Training loss (mean squared error) as a function of epoch number, showing stable convergence after approximately 600 epochs. (e) Comparison between predicted values and ground truth for the test dataset, yielding a mean absolute error of 0.04 and a root mean square error of 0.06, demonstrating accurate recognition, and robust generalization capability.

The electrical outputs of the photodetector under structured red and green illumination were organized into two-dimensional arrays and used as the direct input for learning-based recognition. To assess the robustness of the system against spatial misalignment, detector readouts corresponding to centered optical patterns were employed for training, whereas spatially shifted patterns were used exclusively for testing, mimicking practical scenarios in which optical signals are not perfectly aligned with the sensor (Figure 5b). More specifically, the training set consists of two groups of original standard digit traffic-light data. Based on these two datasets, data augmentation was applied by adding random noise to the original data patterns, resulting in a total of ten groups of training data. The test set comprises one group of real, spatially shifted data.

Given the relatively small magnitude of the raw photocurrent signals, a lightweight preprocessing step with a learnable scaling factor was applied to normalize the detector outputs and enhance feature contrast. The processed data were subsequently passed through a convolutional feature extraction module to capture spatial correlations and shape-related characteristics, followed by a compact fully connected network for final classification (Figure 5c). We also compared a standard multilayer perceptron (MLP) for feature extraction and found that, under the same architecture, it converges more slowly than the convolution-based feature extractor. Details can be found in the Figure S16. This architecture enables end-to-end recognition directly driven by physical photoresponses of the device, rather than by artificially generated images.

The training was conducted with a batch size of 8 and 600 epochs. The initial learning rate was set to 1e-4, and the Adam optimizer was used. During training, the model exhibits stable convergence behavior, with the loss function decreasing monotonically and approaching a low steady-state value after sufficient epochs, indicating effective learning of the underlying

16163028, 2026, 71, Downloaded from https://advanced.onlinelibrary.wiley.com/doi/10.1002/adfm.77559 by Beihang University (Buaa), Wiley Online Library on [23/09/2026]. See the Terms and Conditions (https://onlinelibrary.wiley.com/terms-and-conditions) on Wiley Online Library for rules of use; OA articles are governed by the applicable Creative Commons License

features (Figure 5d). To quantitatively evaluate the recognition accuracy and generalization capability, numerical patterns with different colors were encoded into distinct value ranges, allowing simultaneous discrimination of color and shape information.

When tested using spatially shifted inputs that were not included in the training set, the model maintains a low prediction error, demonstrating strong generalization ability. The predicted outputs show excellent agreement with the ground truth values, yielding a mean absolute error of 0.04 and a root mean square error of 0.06 (Figure 5e). These results confirm that the model captures intrinsic geometric features rather than memorizing fixed pixel-level responses.

Collectively, this device-algorithm co-designed framework demonstrates that the $MoS_2/MAPbBr_3$ photodetector can serve as an optoelectronic sensing front end for signal encoding, capable of providing distinguishable electrical signals that can be processed for optical signal classification. It should be noted that the classification is performed by the CNN model, while the device serves as a physical signal encoder that generates distinguishable temporal responses. The present implementation is limited to predefined discrete inputs and does not address mixed spectral conditions.

3 | Conclusion

In summary, we demonstrated a large-area $MoS_2/MAPbBr_3$ perovskite van der Waals heterojunction photodetector featuring a distinctly wavelength-dependent dual-mode photoresponse. Under green-light excitation, the device exhibits a stable photoconductive current dominated by carrier generation and transport in the MoS_2 channel. In contrast, red-light illumination induces a pronounced transient current originating from thermally induced modulation of the interfacial electronic structure at the $MoS_2/MAPbBr_3$ heterointerface. The temporal and spectral decoupling of these two response modes, achieved via distinct electrical signatures, enables intrinsic optical logic discrimination at the device level. This work demonstrates a feasible approach for achieving wavelength-dependent signal differentiation by integrating photoconductive processes with thermally induced interfacial modulation in hybrid low-dimensional heterostructures. The proposed approach paves the way for compact, energy-efficient, and wavelength-selective photodetectors applicable to next-generation sensing, imaging, and signal classification systems.

4 | Experimental Section

4.1 | Synthesis of CVD-Grown MoS_2 Films

In the three-temperature zone tubular furnace, MoS_2 films were synthesized using a C-plane sapphire substrate. The substrate was placed face-up on a quartz plate located in the heating zone. For the S and Mo precursors, sulfur powder and MoO_3 were used respectively. These powders were placed in two separate quartz boats to avoid cross-contamination or Mo source poisoning. The two precursors were independently heated in the upstream low-temperature zone of the furnace. Before growth, the chamber was evacuated to a basic pressure of approximately 3 Pa. Subsequently, a carrier gas was introduced and the furnace was ramped to the target growth temperature over 50 min. At this temperature, it was maintained for another 40 min to ensure complete film growth. Finally, the furnace was allowed to cool naturally to room temperature.

4.2 | Preparation of $MAPbBr_3$ Precursor Solution

The $MAPbBr_3$ precursor solution (0.8 M) was prepared by dissolving the precursors in a mixed solvent of DMF/DMSO/acetonitrile (ACN) with a volume ratio of 4:1:2. Specifically, methylammonium bromide (MABr, 125.4 mg), lead bromide ($PbBr_2$, 411.1 mg), and L-ascorbic acid (L-AA, 9.9 mg, corresponding to 5 mol% with respect to Pb^{2+}) were dissolved in 1.4 mL of the mixed DMF/DMSO/ACN solvent under stirring to form a homogeneous precursor solution.

4.3 | Fabrication of MoS_2 Photodetector Devices

First, the bottom cross electrode pattern is fabricated on the SiO_2/Si substrate through lithography, and then the bottom electrode is prepared by magnetron sputtering. Cr/Au electrodes were deposited by magnetron sputtering under a high vacuum of 5×10^{-5} Pa with an Ar atmosphere, using a sputtering power of 70 W. Cr and Au were sputtered for 1 and 5 min, respectively, ensuring firm adhesion of the metal contacts to the substrate. Following electrode fabrication, the material was positioned via a localized transfer process.

Using the potassium hydroxide-assisted peeling technique, the molybdenum disulfide film was transferred onto the chromium/gold cross electrodes on the SiO_2/Si substrate. The specific operation was as follows: 1.5 g of polystyrene (PS) was dissolved in 8.5 g of toluene, and then spin-coated onto the sample at a speed of 2000 rpm for 1 min. It was then baked at 120°C for 5 min. A polydimethylsiloxane (PDMS) template was used as the supporting layer, and the PS on the edge of the sapphire was gently scraped off to allow the moisture to penetrate. The stacked structure was immersed in a 1 M potassium hydroxide solution and soaked at 65°C for approximately 2 h to etch the sapphire interface. After the peeling of the MoS_2 film/PS/PDMS stacked structure, it was rinsed in deionized water and then transferred to the Cr/Au patterned Si/SiO_2 target substrate. The PDMS was removed by heating to 130°C, and then PS was dissolved in toluene after cooling, leaving a clean MoS_2 film precisely aligned in the expected device area.

4.4 | Fabrication of $MoS_2/MAPbBr_3$ Photodetector Devices

Align and place a 1 cm laser-cut shadow mask above the MoS_2 channel to ensure that the masked area remains smaller than the active MoS_2 area. Then, fill a spraying nozzle with 70 μL of $MAPbBr_3$ precursor solution. Place the MoS_2 device on a 110°C hot plate and slowly and evenly spray the precursor onto the exposed area to form a spray-coated $MAPbBr_3$ layer within the mask-defined region. Subsequently, heat the sample

16163028, 2026, 71, Downloaded from https://advanced.onlinelibrary.wiley.com/doi/10.1002/adfm.77559 by Beihang University (Buaa), Wiley Online Library on [23/09/2026]. See the Terms and Conditions (https://onlinelibrary.wiley.com/terms-and-conditions) on Wiley Online Library for rules of use; OA articles are governed by the applicable Creative Commons License

at 110°C for 20 min to promote solvent evaporation, facilitate the crystallization of the perovskite grains, and improve the interface contact between $MAPbBr_3$ and MoS_2.

4.5 | Electrical Measurement

The photoresponse of the device was characterized by using a 520 and 650 nm laser as the light source. The *I–V* and *I–t* curves of the device were tested under dark conditions and different light intensities by a current amplifier (Stanford SR570), a function generator (Stanford DS345), and a probe station (Semiprobe M-6). The *I–t* measurements were performed at a fixed drain-source bias (V_{ds}) of 1 V.

Acknowledgements

The authors thank the support of National Key Research and Development (R&D) Program from Ministry of Science and Technology of China (2021YFA1400502 and 2024YFB3814100), National Natural Science Foundation of China (No. 52125205, 52532005, 52250398, 52172035, U25A20483, and 52203307), Natural Science Foundation of Beijing Municipality (2222088 and L223006), and the Fundamental Research Funds for the Central Universities. The authors also thank Xuzhou B&C Chemical Co. Ltd for providing the photoresist (HTA116, HTA112, B&C Chemicals) used in our work.

Conflicts of Interest

The authors declare no conflicts of interest.

Data Availability Statement

The data that support the findings of this study are available from the corresponding author upon reasonable request.

References

1. Y. Fan, W. Huang, F. Zhu, et al., "Dispersion-Assisted High-Dimensional Photodetector," *Nature* 630 (2024): 77–83.

2. W. Ran, Z. Ren, P. Wang, et al., "Integrated Polarization-Sensitive Amplification System for Digital Information Transmission," *Nature Communications* 12 (2021): 6476.

3. Z. Xu, X. Han, W. Wu, et al., "Controlled On-Chip Fabrication of Large-Scale Perovskite Single Crystal Arrays for High-Performance Laser and Photodetector Integration," *Light: Science & Applications* 12 (2023): 67.

4. J. Meng, Q. Li, J. Huang, C. Pan, and Z. Li, "Self-Powered Photodetector for Ultralow Power Density UV Sensing," *Nano Today* 43 (2022): 101399.

5. W. Wu, H. Lu, X. Han, et al., "Recent Progress on Wavelength-Selective Perovskite Photodetectors for Image Sensing," *Small Methods* 7 (2023): 2201499.

6. T. Wang, K. Andrews, A. Bowman, et al., "High-Performance WSe_2 Phototransistors With 2D/2D Ohmic Contacts," *Nano Letters* 18 (2018): 2766–2771.

7. Y. Peng, J. Lu, X. Wang, et al., "Self-Powered High-Performance Flexible GaN/ZnO Heterostructure UV Photodetectors With Piezo-Phototronic Effect Enhanced Photoresponse," *Nano Energy* 94 (2022): 106945.

8. S. Zhang, H. Jiao, Y. Chen, et al., "Multi-Dimensional Optical Information Acquisition Based on a Misaligned Unipolar Barrier Photodetector," *Nature Communications* 15 (2024): 7071.

9. X. Pan, J. Li, Z. Xu, et al., "A High Stretchability Micro-Crack Tactile Sensor System Based on Strain-Isolation Substrate," *Materials Today Physics* 48 (2024): 101562.

10. J. He, R. Wei, S. Ge, et al., "Artificial Visual-Tactile Perception Array for Enhanced Memory and Neuromorphic Computations," *InfoMat* 6 (2023): 12493.

11. L. Bai, Z. Yang, J. Wen, et al., "Polarization Reversal Enhanced Intelligent Recognition in Two-Dimensional $MoTe_2$/GeSe Heterostructure," *Chip* 4 (2025): 100143.

12. C. Han, J. Han, L. Guo, et al., "Retina-Inspired Dual-Mode Photodetector with Spectral-Tunable Memory Switching for Neuromorphic Visual Systems," *ACS Photonics* 12 (2025): 2169.

13. L. Bian, Z. Wang, Y. Zhang, et al., "A Broadband Hyperspectral Image Sensor With High Spatio-Temporal Resolution," *Nature* 635 (2024): 73–81.

14. G. Konstantatos and E. H. Sargent, "Nanostructured Materials for Photon Detection," *Nature Nanotechnology* 5 (2010): 391–400.

15. Q. Wang, Q. Zhang, X. Luo, et al., "Optoelectronic Properties of a Van Der Waals WS_2 Monolayer/2D Perovskite Vertical Heterostructure," *ACS Applied Materials & Interfaces* 12 (2020): 45235–45242.

16. J. Tang, Q. Wang, J. Tian, et al., "Low Power Flexible Monolayer MoS_2 Integrated Circuits," *Nature Communications* 14 (2023): 3633.

17. Z. Yang, S. Huo, Z. Zhang, et al., "High-Precision Multibit Opto-Electronic Synapses Based on ReS_2/h-BN/Graphene Heterostructure for Energy-Efficient and High-Accuracy Neuromorphic Computing," *Advanced Functional Materials* 35 (2025): 2509119.

18. P. Chen, J. Pan, W. Gao, et al., "Anisotropic Carrier Mobility From 2H WSe_2," *Advanced Materials* 34 (2022): 2108615.

19. Q. Zhang, S. Zuo, P. Chen, and C. Pan, "Piezotronics in Two-Dimensional Materials," *InfoMat* 3 (2021): 987.

20. J. Song, T. Li, W. Li, et al., "Enabling Fast Photoresponse in Hybrid Perovskite/MoS_2 Photodetectors by Separating Local Photocharge Generation and Recombination," *Nano Letters* 24 (2024): 14307–14314.

21. J. Tang, X. Wang, J. Zhang, et al., "A Chalcogenide-Cluster-Based Semiconducting Nanotube Array With Oriented Photoconductive Behavior," *Nature Communications* 12 (2021): 4275.

22. X. Z. Hu, J. Li, H. Z. Ji, Q. F. Ren, X. M. Luo, and S. Q. Zang, "Achieving Dark Current Suppression and Photocurrent Enhancement Simultaneously in 2D MoS_2 Photodetector via Ag 70 Nanocluster Modification," *Nano Research* 19 (2026): 94907805.

23. H. Wang, X. Wang, Y. Chen, et al., "Extremely Low Dark Current MoS_2 Photodetector via 2D Halide Perovskite as the Electron Reservoir," *Advanced Optical Materials* 8 (2020): 1901402.

24. X. Song, X. Liu, D. Yu, et al., "Boosting Two-Dimensional MoS_2/$CsPbBr_3$ Photodetectors via Enhanced Light Absorbance and Interfacial Carrier Separation," *ACS Applied Materials & Interfaces* 10 (2018): 2801–2809.

25. Z. He, B. Sun, H. Lu, et al., "Focus-Tunable Real-Time Imaging System Based on Ultrathin Perovskite Curved Image Sensor With Hierarchical Mesh Design," *Science Advances* 11 (2025): adw7826.

26. J. Sun, T. Li, L. Dong, et al., "Excitation-Dependent Perovskite/Polymer Films for Ultraviolet Visualization," *Science Bulletin* 67 (2022): 1755.

27. Z. Yang, H. Wang, L. Guo, et al., "A Self-Powered Photodetector Based on $MAPbI_3$ Single-Crystal Film/n-Si Heterojunction With Broadband Response Enhanced by Pyro-Phototronic and Piezo-Phototronic Effects," *Small* 17 (2021): 2101572.

28. N. M. Gabor, J. C. W. Song, Q. Ma, et al., "Hot Carrier–Assisted Intrinsic Photoresponse in Graphene," *Science* 334 (2011): 648–652.

29. X. Xu, N. M. Gabor, J. S. Alden, A. M. van der Zande, and P. L. McEuen, "Photo-Thermoelectric Effect at a Graphene Interface Junction," *Nano Letters* 10 (2010): 562–566.

30. L. Guo, H. Wang, Z. Xu, et al., "Interfacial Pyro-Phototronic Effect: A Universal Approach for Enhancement of Self-Powered Photodetection Based on Perovskites With Centrosymmetry," *Advanced Functional Materials* 33 (2023): 2306526.

16163028, 2026, 71, Downloaded from https://advanced.onlinelibrary.wiley.com/doi/10.1002/adfm.77559 by Beihang University (Buaa), Wiley Online Library on [23/09/2026]. See the Terms and Conditions (https://onlinelibrary.wiley.com/terms-and-conditions) on Wiley Online Library for rules of use; OA articles are governed by the applicable Creative Commons License

31. K. Liao, K. Ding, S. Li, et al., "Enhanced Near-Infrared Photodetection in a Mixed-Dimensional 0D/2D Heterostructure via Two-Photon Absorption," *Laser & Photonics Reviews* 19 (2025): 2401352.

32. Z. Xu, Y. Zeng, F. Meng, et al., "A High-Performance Self-Powered Photodetector Based on $MAPbBr_3$ Single Crystal Thin Film/MoS_2 Vertical Van Der Waals Heterostructure," *Advanced Materials Interfaces* 9 (2022): 2200912.

33. A. Yang, J. C. Blancon, W. Jiang, et al., "Giant Enhancement of Photoluminescence Emission in WS_2-Two-Dimensional Perovskite Heterostructures," *Nano Letters* 19 (2019): 4852–4860.

34. Y. Liang, Q. Lu, W. Wu, et al., "A Universal Fabrication Strategy for High-Resolution Perovskite-Based Photodetector Arrays," *Small Methods* 7 (2023): 2300339.

35. Y. Chen, J. Ma, Z. Liu, J. Li, X. Duan, and D. Li, "Manipulation of Valley Pseudospin by Selective Spin Injection in Chiral Two-Dimensional Perovskite/Monolayer Transition Metal Dichalcogenide Heterostructures," *ACS Nano* 14 (2020): 15154–15160.

36. F. Zu, R. Wang, L. Frohloff, et al., "Light-Induced Electronic Band Realignment at the Metal Halide Perovskite/Monolayer MoS_2 Heterojunction," *ACS Applied Materials & Interfaces* 17 (2025): 30251–30258.

37. S. Das, H. Y. Chen, A. V. Penumatcha, and J. Appenzeller, "High Performance Multilayer MoS_2 Transistors With Scandium Contacts," *Nano Letters* 13 (2013): 100–105.

38. H. Yang, S. Cai, Y. Zhang, D. Wu, and X. Fang, "Enhanced Electrical Properties of Lithography-Free Fabricated MoS_2 Field Effect Transistors With Chromium Contacts," *The Journal of Physical Chemistry Letters* 12 (2021): 2705–2711.

39. M. Bernardi, M. Palummo, and J. C. Grossman, "Extraordinary Sunlight Absorption and One Nanometer Thick Photovoltaics Using Two-Dimensional Monolayer Materials," *Nano Letters* 13 (2013): 3664–3670.

40. F. Meng, Z. Xu, Y. Zeng, et al., "Photodetectors Based on MoS_2/$MAPbBr_3$ van der Waals Heterojunction," *IEEE Electron Device Letters* 43 (2022): 414–417.

41. O. Lopez-Sanchez, D. Lembke, M. Kayci, A. Radenovic, and A. Kis, "Ultrasensitive Photodetectors Based on Monolayer MoS_2," *Nature Nanotechnology* 8 (2013): 497–501.

42. R. Nur, T. Tsuchiya, K. Toprasertpong, K. Terabe, S. Takagi, and M. Takenaka, "High Responsivity in MoS_2 Phototransistors Based on Charge Trapping HfO_2 Dielectrics," *Communications Materials* 1 (2020): 103.

43. A. Bayou, B. Asbani, N. Rajput, et al., "Unlocking Superior Photodetection Properties of Electrodeposited MoS_2 Quantum Dots," *Small* 21 (2025): 08001.

44. A. Di Bartolomeo, A. Kumar, O. Durante, et al., "Temperature-Dependent Photoconductivity in Two-Dimensional MoS_2 Transistors," *Materials Today Nano* 24 (2023): 100382.

45. S. Touili, M. Amjoud, D. Mezzane, et al., "An Overview of Low-Carbon Hydrogen Production via Water Splitting Driven by Piezoelectric and Pyroelectric Catalysis," *International Journal of Hydrogen Energy* 78 (2024): 218–235.

46. A. J. Gabourie, Ç. Köroğlu, and E. Pop, "Substrate-Dependence of Monolayer MoS_2 Thermal Conductivity and Thermal Boundary Conductance," *Journal of Applied Physics* 131 (2022): 195103.

47. B. Wu, M. Zhou, D. Xu, J. Liu, R. Tang, and P. Zhang, "Interfacial Thermal Conductance of BP/MoS_2 Van Der Waals Heterostructures," *Surfaces and Interfaces* 32 (2022): 102119.

48. C. Wang, B. R. Ecker, H. Wei, J. Huang, and Y. Gao, "Environmental Surface Stability of the $MAPbBr_3$ Single Crystal," *The Journal of Physical Chemistry C* 122 (2018): 3513–3522.

49. C. C. Stoumpos and M. G. Kanatzidis, "The Renaissance of Halide Perovskites and Their Evolution as Emerging Semiconductors," *Accounts of Chemical Research* 48 (2015): 2791–2802.

50. A. Jha, H. Shankar, S. K. Saini, M. Kumar, and P. Kar, "Probing the Electron Transfer Behavior from Excited State Organometal Lead Halide Perovskite Nanocrystals to Molybdenum Disulfide Nanoflowers," *ACS Applied Nano Materials* 6 (2023): 8453–8460.

Supporting Information

Additional supporting information can be found online in the Supporting Information section.

Supporting File 1: adfm77559-sup-0001-SuppMat.docx

16163028, 2026, 71, Downloaded from https://advanced.onlinelibrary.wiley.com/doi/10.1002/adfm.77559 by Beihang University (Buaa), Wiley Online Library on [23/09/2026]. See the Terms and Conditions (https://onlinelibrary.wiley.com/terms-and-conditions) on Wiley Online Library for rules of use; OA articles are governed by the applicable Creative Commons License